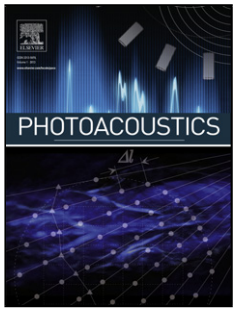

Title: Fluence compensation in raster-scan optoacoustic angiography

Authors: Mikhail Kirillin, Valeriya Perekatova, Ilya Turchin, Pavel Subochev

PII: S2213-5979(17)30024-1
DOI: http://dx.doi.org/10.1016/j.pacs.2017.09.004
Reference: PACS 83

To appear in:

Received date: 17-5-2017
Revised date: 25-8-2017
Accepted date: 13-9-2017

Please cite this article as: {http://dx.doi.org/

Fluence compensation in raster-scan optoacoustic angiography

Mikhail Kirillin, Valeriya Perekatova*, Ilya Turchin, and Pavel Subochev

Institute of Applied Physics, Russian Academy of Sciences, 46 Ulyanov Street, Nizhny Novgorod 603950, Russia

Abstract

Modern optical imaging techniques demonstrate significant potential for high resolution *in vivo* angiography. Optoacoustic angiography benefits from higher imaging depth as compared to pure optical modalities. However, strong attenuation of optoacoustic signal with depth provides serious challenges for adequate 3D vessel net mapping, and proper compensation for fluence distribution within biotissues is required. We report on the novel approach allowing to estimate effective in-depth fluence profiles for optoacoustic systems. Calculations are based on Monte Carlo simulation of light transport and account for complex illumination geometry and acoustic detection parameters. The developed fluence compensation algorithm was tested in *in vivo* angiography of human palm and allowed to overcome significant in-depth attenuation of probing radiation and enhance the contrast of lower dermis plexus while preserving high resolution of upper plexus imaging.

Abbreviations

RSOM – Raster-scan optoacoustic mesoscopy

***Keywords*:** Optoacoustic imaging; Fluence compensation; Monte Carlo simulations.

***Valeriya Perekatova, E-mail: ValeriyaPerekatova@gmail.com FP – focus position

OA – optoacoustic

1. Introduction

Biomedical optoacoustic (OA) or photoacoustic imaging is a hybrid modality combining the benefits of optical contrast and ultrasonic resolution [1]. Raster scan optoacoustic mesoscopy (RSOM) [2, 3] is a rapidly emerging technology [4] which employs confocal optical illumination and acoustic detection [5]. Due to high absorption of blood as compared to surrounding biotissues in visible range OA imaging is extremely efficient for *in vivo* angiography [6] with spatial resolution below 100 μm at millimeter depths. However, strong scattering and absorption in biotissues result in rapid in-depth attenuation of probing laser radiation and limit the diagnostic depth of RSOM imaging [7].

In order to overcome this disadvantage of RSOM bioimaging, the compensation of fluence distribution is required [8, 9]. Typical approach to fluence correction consists in calculation or measurement of the probing radiation distribution within medium and calculating the ratio of raw optoacoustic signal from the image voxel and probing radiation fluence within this voxel [10] thus providing the actual local absorption coefficient [11].

The optical fluence can be reconstructed from diffuse optical tomography measurements [10]. Obviously, such approach allow to accurately account for optical macroinhomogeneitites within object, however, it requires additional object inspection by an independent imaging modality. Alternativelly, diffuse reflectance spectroscopy [12], and acousto-optical techiques [13] can be employed, providing, however, smaller accuracy in optical fluence distribution.

Model-based correction for optical fluence is efficiently implemented in OA tomography [14], when illumination system is stationary with respect to the probing tissue [10, 15] [16] and a single calculation can provide distribution of the probing intensity in the entire measurement volume. Model-based calculations can be performed either with Monte Carlo technique [13, 17] or using diffuse equation [18]. Obviously, phantom mesurements ususally demonstrate excellent performance of fluence compensation as optical properties of the inspected objects are controlled and well-known, on the contrary to measuring real biological tissues. In this respect, concept of multiple irradiation sensing [19] is a promising approach since it does not require *a priory* knowledge of tissue optical properties.

Regarding fluence compensation in RSOM imaging techniques, previously quantitative multispectral optoacoustic measurements were performed employing an analytical model based on spectral optoacoustic amplitudes at shallow imaging dephs [20] or in the optical diffuse regime [21].

In the diffusive regime modified Monte Carlo convolution approach [22] has been employed for calculating fluence in axially symmetrical illumination configuration for planar-parallel geometry [15]. Since a scanning head of RSOM system moves along the investigated object, fluence distribution should be calculated or measured for each head position. Alternatively, lateral inhomogeneities rarely distributed within object could be neglected, and a single calculation for planar geometry can be employed for all the positions of scanning optoacoustic head.

In this paper we report on the novel approach to fluence compensation in RSOM phantom measurements and *in vivo* angiography. Each A-scan of the resulting *in vivo* 3D OA image is normalized by 1D array of effective fluence distribution derived from full 3D Monte Carlo simulation with optical parameters close to those of inspected biotissue accounting for the geometry of optical illumination and ulstrasonic antenna detection diagram.

2. Materials and Methods

2.1. RSOM system and measurements

Figure 1 presents the schematic of RSOM system for *in vivo* imaging. The geometrical configuration of scanning optoacoustic head provides confocal laser illumination and ultrasonic detection (Fig. 1). The probing fiber bundle consists of 70 optical fibers with 100 μm core diameter and 0.12 numerical aperture used for light delivery to the object. Spherically focused polyvinylidene fluoride detector (35 MHz central frequency, 30 MHz bandwidth, F = 6.7 mm focal distance, and 0.6 numerical aperture) provided 50 μm lateral resolution in phantom experiments with the same system [23].

Lateral movements of OA head across the investigated object (Fig. 1) were controlled by computer-driven XY stages M-664 (PI Micos, Germany). Probing laser pulses were generated by HB532 (BrightSolutions, Italy) laser system at λ =532 nm with maximum repetition rate of 2kHz. Radiant exposure at the palm's surface was kept below

7.5 mJ/cm^2 level in accordance to 20 mJ/cm^2 maximum value allowed by ANSI Z136.1 standard for laser safety. A-scans corresponding to discrete XY positions of the scanning head were recorded by analog-to-digital converter (ADC) CSE1622 (Gage, USA). In order to minimize errors in fluence compensation originating from the biotissue surface roughness, the boundary of the medium was automatically recognized for each B-scan corresponding to the scanning along the X-axis with fixed Y position. Then each A-scan starting from the determined boundary position was compensated for calculated distribution of probing radiation fluence within tissue. Finally, 3D data sets were processed using the reconstruction algorithm [24].

All phantom experiments were performed in a phantom consisted of 14 copper wires with diameter of 30 μm placed in 2% water solution of Intralipid. RSOM B-scans of wires were obtained by mechanical scanning within 7 mm area in X direction with lateral scanning step of 5 μm, used for all the phantom experiments. According to this each B-scan consists of 1400 A-scans. The images were acquired for two different focus position FD = 2.21 mm and FD = 1.1 mm.

All *in vivo* experiments were conducted at the researchers's human palms with caucasian skin and different ages: a 20 year-old male, a 33 year-old male and a 24 year-old female. Arms of healthy human volunteers were fixed in palm-up position and pressed by immersion chamber filled with water. Rectangular hole in the bottom of immersion chamber allowed to provide RSOM scanning within 7.5 mm x 7.5 mm area in XY plane. Lateral scanning step of 25 μm was used for all the *in vivo* experiments. The images were acquired for three different focus positions (on the top of the human palm, 0.5, and 1.5 mm in depth).

2.2. Monte Carlo simulation of fluence distribution

To simulate fluence distribution provided by illumination of RSOM system previously developed Monte Carlo code [25, 26] was adapted. We assumed uniform distribution of incident photons within the infinitely thin ring of radius 4.6 mm corresponding to radial distribution of optical fibers in fiber bundle (Fig.1). The finite 125 μm thickness of the ring was neglected as it was small compared to millimeter distances of the considered geometry (Fig.1). Further, it was assumed that illumination system produces a uniformly illuminated circle with radius of 1.283 mm in the focal plane which corresponds to the profilometry of the experimental probing beam.

The Monte Carlo simulations were performed in a medium with a total thickness of 6 mm, the step in Z direction was 7.5 μm, that corresponds to the time step in OA-scan. The number of the launched photons in each Monte Carlo simulations equaled 10^7.

Since the acquired A-scans correspond to the independent scanning head positions, it is convenient to normalize them by a one dimensional profile of the effective fluence. On the other hand, one should account for detection diagram of the employed focused acoustic antenna, for which collection area strongly depends on the distance from the antenna focal plane. In this respect, it is not correct to average the fluence over the equal areas for different probing depths. To derive the 1D fluence distribution we averaged the fluence at a given depth over the area equal to the cross-section

of the antenna detection diagram at this depth. The shape of the averaging area in lateral direction was assumed to be Gaussian:

$$r(z) = r_0\sqrt{1+\left(\frac{\lambda z}{\pi r_0^2}\right)^2}, \quad (1)$$

where z is the in-depth distance from the focal plane, r is the radius of the corresponding cross-section, r_0 is the waist of the antenna diagram, and λ is the effective detection wavelength. In simulations the parameters were chosen in accordance with characteristics of the employed antenna: $r_0 = 25$ μm, and $\lambda = 62$ μm.

2.3. Optical properties of phantom and human skin

An important part of fluence compensation is the choice of proper optical properties of the inspected medium. They can be easily obtained in model experiments with calibrated media, however, in *in vivo* measurements distribution of the optical properties within medium is quite complex and even knowing the exact tissue geometry may produce discrepance due to inaccuracy in choosing particular optical properties value. In this situation averaged optical properties may produce the desirable result. Optical properties of skin in the spectral range of 500-600 nm from two review papers are summarized in Table 1.

The input parameters for Monte Carlo simulations of fluence distribution for human skin were chosen as averaged values of those summarized in Table 1 optical properties. Basing on these reported values the following optical properties of dermis were selected for calculation: $\mu_s = 10$ mm^{-1}, $\mu_a = 0.3$ mm^{-1}, $g = 0.8$, $n = 1.37$.

For Monte Carlo simulations in phantom the optical properties of 2% aqueous solution of Intralipid [29] were reconstructed from spectrophotometry measurements with Analytik Jena Specord 250Plus system (Germany). The obtained values at the wavelength of 532 nm are $\mu_s = 5.37$ mm^{-1}, $\mu_a = 0.057$ mm^{-1}, $g = 0.631$.

3. Results and Discussion

3.1. Monte Carlo simulation of axial fluence distribution

The simulations of effective fluence distribution were performed for various focus positions (FP) used during *in vivo* experiments. In order to demonstrate the importance of the introduced features of the developed approach, we compared the resulting 1D profiles of fluence with simplified results corresponding to point beam illumination, flat beam illumination, and situation when fluence averaging is performed over the equal areas at all considered depths. Considered combinations of optical illumination geometry and averaging determined by the acoustic antenna diagram are shown in Fig. 2.

Figure 3 demonstrates axial distributions of fluence within model medium for configurations g,h, and i from Fig.2 for two FPs: focus is on the surface of the medium and focus is 2.5 mm under the surface of the medium. In the case when the optical focus of the scanning system is located on the sample surface the in-depth fluence decay is very close

to exponential, which is usually employed for compensation [30]. However, when the focus is within the object, in the superficial layer the fluence distribution drastically differs from the exponential. It is also evident, that avegaring area significantly affects the result when the focus is 2.5 mm under the surface, hence, account for anetenna diagram shape is important in this situation.

The fluence distribution calculated for configuration *g* (further addressed as RSOM distribution) was also compared to fluence calculated for point-size monodirectional beam (conf. *a*-*c*) and for flat distribution of the probing intensity equivalent to probing with a planar wave (conf. *d*-*f*). The results aiming to demonstrate the effect of illumination geometry are shown in Fig. 4. Point beam illumination, as expected, produces extremely high values close to the surface, especially when averaging is performed over the small area concentric with the beam axis (conf. *a*). In general, results for point-beam illumination geometry strongly depend on averaging and significantly differ from RSOM distribution. Fluence distribution for flat illumunation (conf. *d*-*f*) does not depend on averaging and is much closer to RSOM distribution, however, it still differs indicating that RSOM distribution employment is critical for proper quantitative correction.

Figure 5 demonstrates RSOM fluence distributions (conf. *i*) for different in-depth positions of the illumination system focus. As it was already demonstrated earlier, when the focus is close to the surface the dependence is extremely close to exponential decay, however, starting from FP=1.5 mm the distribution significantly differs from the exponential for smaller depths under the object surface. Additionally, distribution slope at larger depth also differs for different FPs.

3.2. Fluence compensation in OA imaging of phantoms

Firstly, the developed approach was applied to measurements of the phantom consisting of Intralipid solution with embedded absorbing wires. The results of application of fluence compensation to phantom images are demonstrated in Figure 6: optoacoustic raw B-scan of phantom for focus position FD = 2.21 mm is shown in Fig. 6 a, while the results of fluence compensation are shown in Figs. 6 b-f. From raw B-scans one can clearly see that the signals from superficial wires are high while deep laying wires cannot be distinguished due to strong in-depth signal attenuation (Fig. 6 a). However, application of fluence compensation significantly improves images resulting in much higher contrast to deeper laying wires (Fig. 6 b).

The effect of compensation depends on the chosen optical properties. For the most efficient fluence compensation the native values of tissue optical properties should be used for calculating fluence distribution. In order to demonstrate how the image quality is changing with variations of optical properties we performed fluence compensation with Monte Carlo-derived fluence in-depth distributions for 50 % variations of μ_a and μ_s above and below the reconstructed values for phantom. The chosen optical parameters are presented in Table 2: the native optical parameters are shown as bold.

As we can see from Fig. 6, the Monte Carlo-derived fluence distributions allows to improve contrast of deep laying wires, even if the selected optical parameters differ from the ones considered as native (Fig 6 c-f), however,

variations of μ_a and μ_s distorts the image of wires located on the surface. Meanwhile, Monte Carlo derived fluence distribution for the native values of optical properties allows to obtain the contrast simultaneously for superficial and deep laying wires (Fig. 6 b). Note that the understated optical properties with respect to the native values produce smaller effect to the reconstructed image in comparison to the exceeding values.

In order to demonstrate the role of focus position in fluence compensation we acquired RSOM images of the phantom (Fig. 7 a, d) for two different in-depth positions of the illumination system focus FD = 1.1 mm (Fig. 7 a) and FD = 2.21 mm (Fig. 7 d). The central column of Fig. 7 (b, e) demonstrates images compensated for exponential fluence distribution that corresponds to the modeling for FD = 0 mm when the dependence is close to exponential decay. The Figures 7 b, e demonstrate that compensation for exponential dependence significantly improves images giving much higher contrast to deeper laying wires at depths of 3.5 mm and 4.5 mm (Fig. 7 b, e) which are not distinguished in uncompensated images. However, exponential compensation significantly decreases the signal from superficial layers resulting in almost complete disappearance of the superficial wires (Fig. 7 e) as compared to (Fig. 7 d). The third column of Fig. 7 (c, f) demonstrates the compensated images by RSOM fluence distribution calculated for corresponding focus positions FD = 1.1 mm (Fig. 7 c) and FD = 2.21 mm (Fig. 7 f). As it was previously shown in Fig. 4, fluence distribution for focus positions (FP = 0 mm, FP = 1 mm) are extremely close to exponential, which leads to the similar results of compensation for exponential function (Fig. 7 b) and compensation with fluence calculated for corresponding focus depth (Fig. 7 c). However, for deeper focus position (Fig. 7 f) compensation to RSOM fluence distribution provides much better results compared to compensation for exponential: there are no distortions of the wires located at smaller depths (Fig. 7 f).

3.3. Fluence compensation in OA mesoscopy imaging of human skin

Next, the fluence compensation approach was applied to OA images of human palm *in vivo*. The first column of Fig. 8 (a, d, g, j) demonstrates uncorrected depth-color-encoded OA images of human palm vasculature with FP on the tissue surface (a), at the depth of 0.5 mm (d) and at the depth of 1.5 mm (g, j) obtained by the RSOM system. Note, that figures 8 a and 8 d are obtained from the same site with different FPs. One can see that in these images the signal from superficial skin layers manifested by blue palette vessel net prevails due to strong in-depth signal attenuation. Note, that for smaller focus depths the entire image depth range is smaller.

The second column of Fig. 8 (b, e, h, k) demonstrates corresponding images compensated for exponential distribution (Fig. 5, FP = 0 mm). One can see that this compensation significantly improves images giving much higher contrast to deeper laying vessels. However, for deeper focus position of 1.5 mm (Fig. 8 h, k) exponential compensation produces noise manifested by white points originating from amplification of noise signal from greater depths after fluence compensation. Additionally, exponential compensation significantly decreases the signal from superficial layers resulting in almost complete disappearance of this upper vasculature as compared to uncompensated images. It should be noted that due to surface roughness small blood vessels displayed in yellow in uncompensated images Fig. 8 (a, d, g, j) are actually closer to the surface than the depth reads in the OA image. However fluence

compensation in combination with automated boundary detection, similar to approach reported in [30], allowed to correctly display the depth of blood vessels.

The third column of Fig. 8 (c, f, i, l) demonstrates the images compensated by RSOM fluence distribution calculated for corresponding illumination system focus position. As it can be seen from Fig. 4, fluence distribution for superficial focus positions (FP = 0 mm, FP = 1 mm) are very close to exponential, which results in images extremely similar to ones obtained for exponential compensation (Fig. 8 c, f). However, for deeper focus position (Fig. 8 i, l) compensation to RSOM fluence distribution provides much better results compared to compensation for exponential: noise component is significantly suppressed and upper vasculature becomes more visible.

To conclude, we demonstrated that for considered RSOM configuration fluence compensation allows to significantly improve image quality and enhance contrast of deep laying vessels. For focus position near surface fluence distribution has exponential character, however, when focus is embedded deeper into the tissue, the fluence distribution significantly differs from exponential and accurate Monte Carlo calculation accounting for illumination geometry and acoustic antenna configuration is critical. More than that, considered configuration does not employ sharply focused optical beam (probing beam waist is 1.283 mm in radius); in the case of a sharper focused beam accurate account for beam and antenna geometry becomes even more critical, especially for quantitative optoacoustic imaging.

In order to more evidently demonstrate the results of the proposed compensation algorithm we separately built the images of human vessel net at particular depths before and after fluence compensation for the case when the focus position is 1.5 mm. The depth-color-encoded RSOM images of human palm vasculature are shown in the entire depth range (Fig. 9 a, b), in the depth range of 0.5-1.5 mm (Fig. 9 c, d) and in the depth range of 1.0-1.5 mm (Fig. 9 e, f). One can see that when shifting to deeper range the contrast of deeper laying vessels enhances significantly thus providing additional information about the entire vessel net.

Finally, it is worth mentioning an advantage of the presented RSOM angiography approach against optical angiography. One of the rapidly emerging technologies for high-resolution blood vessel mapping is optical coherence tomography angiography (OCT-A) alose referred as optical coherence angiography [31-33] based on optical coherence tomography technique providing angiographic images with resolution down to units of microns at depths up to 2 mm. However, a drawback of this approach consists in so-called shadowing effect when a shadow appears in the image below blood vessel originating from stronger absorption in blood vessels with respect to neighbouring tissues [34], as the technique is based on detection of backscattered probing radition. In RSOM angiography the illumination is perfomed by a much wider beam as compared to that in OCT-A and more uniform volumetric distribution of probing radiation in combination with acoustic detection allows to avoid this effect.

4. Conclusions

In this paper we report on development of novel algorithm for compensation for probing fluence distribution within inspected object in RSOM angiography. Compensation for each A-scan is performed for 1D fluence distribution array

derived from Monte Carlo simulation. Monte Carlo simulation is performed in full 3D accounting for actual complex geometry of the OA illumination system and geometry of the detecting high numerical aperture acoustic antenna. Simulations were performed for medium mimicking human dermis. Application of fluence compensation allowed to significantly increase the contrast of deep vessels thus providing better visualization of the vessel plexus in the entire measurement volume. We demonstrate that even simple medium geometry provides significant enhancement of the image conrtast at higher depths, however, accounting for local inhomogeneitites within tissue has high potential for further contrast improvement.

Funding

Russian Science Foundation project (14-15-00709-П).

Acknowledgements

The authors are thankful to Mr. Maxim Prudnikov for his assistance with in vivo experiments and to Dr. Michael Jaeger for provision of reconstruction algorithm, Daria Loginova for the assistance in spectrophotometry measurements. Dr. Pavel Subochev acknowledges support from Scholarship of the President of the Russian Federation (project #SP-3196.2016.4).

References

[1] P. Beard, Biomedical photoacoustic imaging, Interface focus 1(4) (2011) 602-631.
[2] J. Aguirre, M. Schwarz, D. Soliman, A. Buehler, M. Omar, V. Ntziachristos, Broadband mesoscopic optoacoustic tomography reveals skin layers, Optics letters 39(21) (2014) 6297-6300.
[3] M. Schwarz, M. Omar, A. Buehler, J. Aguirre, V. Ntziachristos, Implications of ultrasound frequency in optoacoustic mesoscopy of the skin, IEEE transactions on medical imaging 34(2) (2015) 672-677.
[4] M. Omar, D. Soliman, J. Gateau, V. Ntziachristos, Ultrawideband reflection-mode optoacoustic mesoscopy, Optics letters 39(13) (2014) 3911-3914.
[5] H.F. Zhang, K. Maslov, G. Stoica, L.V. Wang, Functional photoacoustic microscopy for high-resolution and noninvasive in vivo imaging, Nature biotechnology 24(7) (2006) 848-851.
[6] J. Yao, L. Wang, J.-M. Yang, K.I. Maslov, T.T. Wong, L. Li, C.-H. Huang, J. Zou, L.V. Wang, High-speed label-free functional photoacoustic microscopy of mouse brain in action, Nature methods 12(5) (2015) 407-410.
[7] J. Yao, L.V. Wang, Photoacoustic microscopy, Laser & photonics reviews 7(5) (2013) 758-778.
[8] B. Cox, J.G. Laufer, S.R. Arridge, P.C. Beard, Quantitative spectroscopic photoacoustic imaging: a review, Journal of biomedical optics 17(6) (2012) 0612021-06120222.
[9] V. Perekatova, P. Subochev, M. Kleshnin, I. Turchin, Optimal wavelengths for optoacoustic measurements of blood oxygen saturation in biological tissues, Biomedical Optics Express 7(10) (2016) 3979-3995.
[10] A.Q. Bauer, R.E. Nothdurft, T.N. Erpelding, L.V. Wang, J.P. Culver, Quantitative photoacoustic imaging: correcting for heterogeneous light fluence distributions using diffuse optical tomography, Journal of Biomedical Optics 16(9) (2011) 096016-096016-7.
[11] P.S. Grashin, A.A. Karabutov, A.A. Oraevsky, I.M. Pelivanov, N.y.B. Podymova, E.V.e. Savateeva, V.S. Solomatin, Distribution of the laser radiation intensity in turbid media: Monte Carlo simulations, theoretical analysis, and results of optoacoustic measurements, Quantum Electronics 32(10) (2002) 868.
[12] J.C. Ranasinghesagara, R.J. Zemp, Combined photoacoustic and oblique-incidence diffuse reflectance system for quantitative photoacoustic imaging in turbid media, Journal of biomedical optics 15(4) (2010) 046016-046016-5.
[13] A. Hussain, K. Daoudi, E. Hondebrink, W. Steenbergen, Mapping optical fluence variations in highly scattering media by measuring ultrasonically modulated backscattered light, Journal of biomedical optics 19(6) (2014) 066002-066002.
[14] X.L. Deán-Ben, A.C. Stiel, Y. Jiang, V. Ntziachristos, G.G. Westmeyer, D. Razansky, Light fluence normalization in turbid tissues via temporally unmixed multispectral optoacoustic tomography, Optics letters 40(20) (2015) 4691-4694.

[15] Z. Xie, L.V. Wang, H.F. Zhang, Optical fluence distribution study in tissue in dark-field confocal photoacoustic microscopy using a modified Monte Carlo convolution method, Applied optics 48(17) (2009) 3204-3211.
[16] F.M. Brochu, J. Brunker, J. Joseph, M.R. Tomaszewski, S. Morscher, S.E. Bohndiek, Towards Quantitative Evaluation of Tissue Absorption Coefficients Using Light Fluence Correction in Optoacoustic Tomography, IEEE Transactions on Medical Imaging (2016).
[17] S. Bu, Z. Liu, T. Shiina, K. Kondo, M. Yamakawa, K. Fukutani, Y. Someda, Y. Asao, Model-based reconstruction integrated with fluence compensation for photoacoustic tomography, IEEE Transactions on Biomedical Engineering 59(5) (2012) 1354-1363.
[18] S. Li, B. Montcel, W. Liu, D. Vray, Analytical model of optical fluence inside multiple cylindrical inhomogeneities embedded in an otherwise homogeneous turbid medium for quantitative photoacoustic imaging, Optics express 22(17) (2014) 20500-20514.
[19] K.G. Held, M. Jaeger, J. Rička, M. Frenz, H.G. Akarçay, Multiple irradiation sensing of the optical effective attenuation coefficient for spectral correction in handheld OA imaging, Photoacoustics (2016).
[20] Z. Guo, S. Hu, L.V. Wang, Calibration-free absolute quantification of optical absorption coefficients using acoustic spectra in 3D photoacoustic microscopy of biological tissue, Optics letters 35(12) (2010) 2067-2069.
[21] Z. Guo, C. Favazza, A. Garcia-Uribe, L.V. Wang, Quantitative photoacoustic microscopy of optical absorption coefficients from acoustic spectra in the optical diffusive regime, Journal of Biomedical Optics 17(6) (2012) 0660111-0660116.
[22] L. Wang, S.L. Jacques, L. Zheng, CONV—convolution for responses to a finite diameter photon beam incident on multi-layered tissues, Computer methods and programs in biomedicine 54(3) (1997) 141-150.
[23] P. Subochev, Cost-effective imaging of optoacoustic pressure, ultrasonic scattering, and optical diffuse reflectance with improved resolution and speed, Optics Letters 41(5) (2016) 1006.
[24] M. Jaeger, S. Schüpbach, A. Gertsch, M. Kitz, M. Frenz, Fourier reconstruction in optoacoustic imaging using truncated regularized inverse k-space interpolation, Inverse Problems 23(6) (2007) S51.
[25] A.V. Gorshkov, M.Y. Kirillin, Acceleration of Monte Carlo simulation of photon migration in complex heterogeneous media using Intel many-integrated core architecture, Journal of Biomedical Optics 20(8) (2015) 085002-085002.
[26] M.Y. Kirillin, G. Farhat, E.A. Sergeeva, M.C. Kolios, A. Vitkin, Speckle statistics in OCT images: Monte Carlo simulations and experimental studies, Optics letters 39(12) (2014) 3472-3475.
[27] A.N. Bashkatov, E.A. Genina, V.V. Tuchin, Optical properties of skin, subcutaneous, and muscle tissues: a review, Journal of Innovative Optical Health Sciences 4(01) (2011) 9-38.
[28] V. Tuchin, Tissue Optics: Light Scattering Methods and Instruments for Medical Diagnosis.
[29] D.A. Loginova, E.A. Sergeeva, A. Krainov, P.D. Agrba, M.Y. Kirillin, Liquid optical phantoms mimicking spectral characteristics of laboratory mouse biotissues, Quantum Electronics 46(6) (2016) 528.
[30] S. Kim, Y.-S. Chen, G.P. Luke, S.Y. Emelianov, In vivo three-dimensional spectroscopic photoacoustic imaging for monitoring nanoparticle delivery, Biomedical optics express 2(9) (2011) 2540-2550.
[31] R.F. Spaide, J.G. Fujimoto, N.K. Waheed, Optical coherence tomography angiography, Retina (Philadelphia, Pa.) 35(11) (2015) 2161.
[32] T.E. De Carlo, A. Romano, N.K. Waheed, J.S. Duker, A review of optical coherence tomography angiography (OCTA), International Journal of Retina and Vitreous 1(1) (2015) 5.
[33] A. Wylęgała, S. Teper, D. Dobrowolski, E. Wylęgała, Optical coherence angiography: A review, Medicine 95(41) (2016).
[34] A.E. Hartinger, A.S. Nam, I. Chico-Calero, B.J. Vakoc, Monte Carlo modeling of angiographic optical coherence tomography, Biomedical optics express 5(12) (2014) 4338-4349.

Valeriya Perekatova (M.Sc., Ph.D. student) is a junior researcher at the Laboratory of Biophotonics of Institute of Applied Physics of Russian Academy of Sciences. She received her Master degree in Physics in 2015 from Lobachevsky State University of Nizhni Novgorod. Her current research focuses on the developing the methods of optoacoustic imaging of biological tissues. Coauthor of 8 peer-review articles and conference proceedings related to optoacostics.

Valeriya Perekatova

Pavel Subochev (Ph.D.) is the optoacoustic group leader at the Laboratory of Biophotonics, Insitute of Applied Physics RAS. He graduated from Lobachevsky State University of Nizhni Novgorod in 2006 and received his PhD in passive acoustic radiometry from the Institute of Applied Physics of Russian Academy of Sciences. Since 2012 he is focused on the development of new instrumentation for optoacousutic imaging of biological tissues. Coauthor of 30 peer-review articles and conference proceedings related to optoacostics.

Pavel Subochev

Mikhail Kirillin (Ph.D., D.Sc.) is a senior researcher at the Laboratory of Biophotonics of Institute of Applied Physics of Russian Academy of Sciences. He graduated with honors from Physics Department of Moscow State University in 2003 and received his PhD degree from the same institution in 2006. In 2008 he received Dr.Sc. (Tech.) degree from University of Oulu. His scientific interests include optics of

biotissues and other scattering media, image formation in tomographic systems including optical coherence and diffusive modalities, techniques for optical clearing and contrast enhancement in tomographic images, as well as theoretical description and numerical simulations (in particular, Monte Carlo technique) of light transport in scattering media. Coauthor of more than 100 peer-review articles, invited and contributed talks, conference proceedings papers, and several book chapters related to laser physics, biomedical optics and laser applications in biology and medicine.

Mikhail Kirillin

Ilya Turchin (Ph.D.) is the Head of the Department for radiophysics methods in medicine at the Institute of Applied Physics of RAS and is an expert in optical imaging systems design (optical diffuse imaging, fluorescence imaging, photoacoustics) and biomedical applications. He has over 10 years of experience as a primary investigator in optical imaging, photodynamic therapy, and translation of optical techniques into clinics. He has published more than 50 peer-review articles.

Ilya Turchin

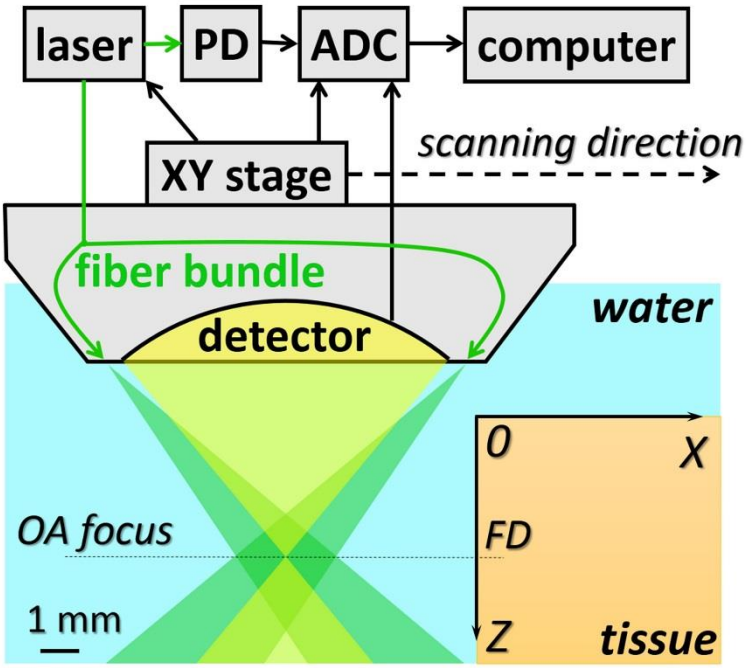

Figure 1: Schematic of RSOM system and geometry of the scanning head.

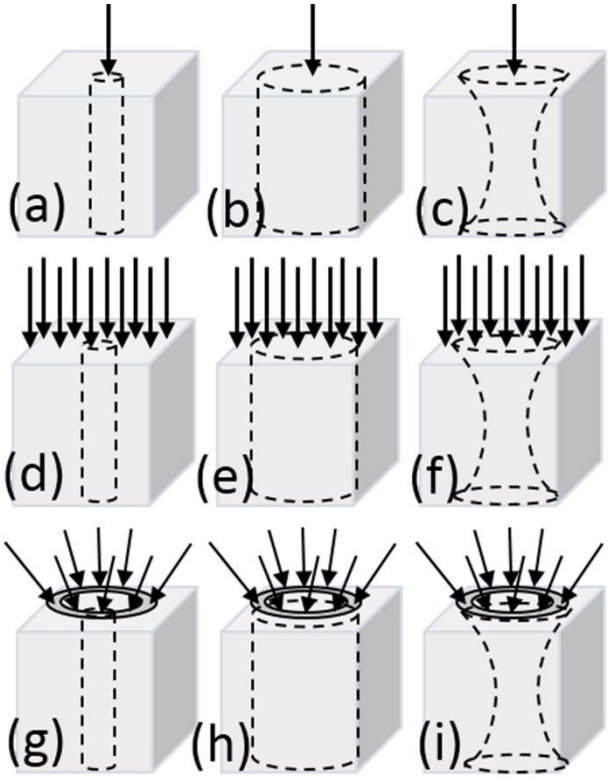

Figure. 2. Considered configurations of the simulation geometry. Arrows show probing optical beam geometry (point beam (a-c), planar wave (d-f), and RSOM illumination (g-i)), dashed line shows acoustic antenna receiving diagram determining averaging area at given depth (circular area with radius of 0.05 mm (antenna diagram waist radius) (a,d,g), with radius of 1.283 mm (beam waist of the RSOM illumination system) (b,e,h) and with variable radius in accordance with formula (1) (Gaussian shape diagram) (c,f,i)).

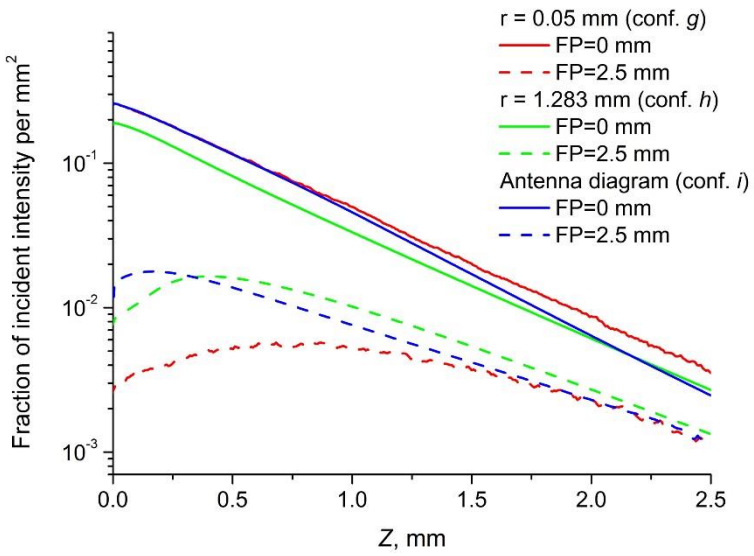

Figure 3: Axial fluence distribution for different focus positions when averaging is performed over the area with radii 0.05 mm (conf. *g*), 1.283 mm (conf. *h*), and over variable area in accordance with antenna diagram (conf. *i*).

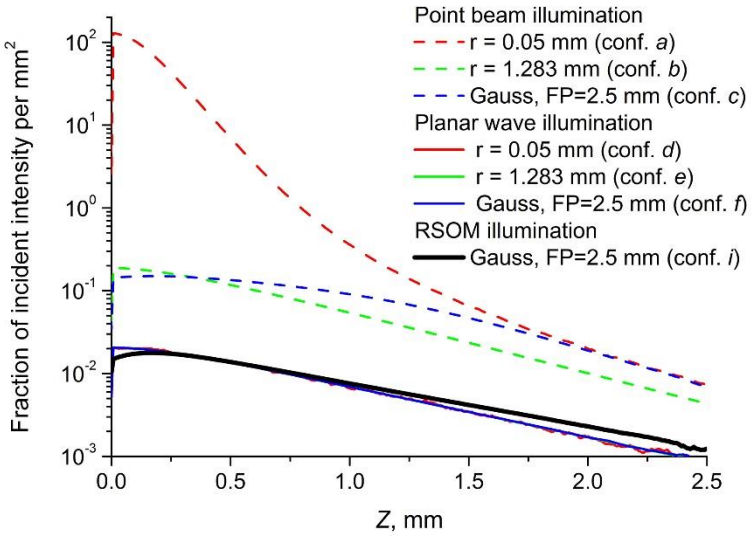

Figure 4: Axial fluence distributions for point-beam (conf. *a-c*) and planar wave (conf. *d-f*) illumination compared to RSOM distribution (conf. *i*).

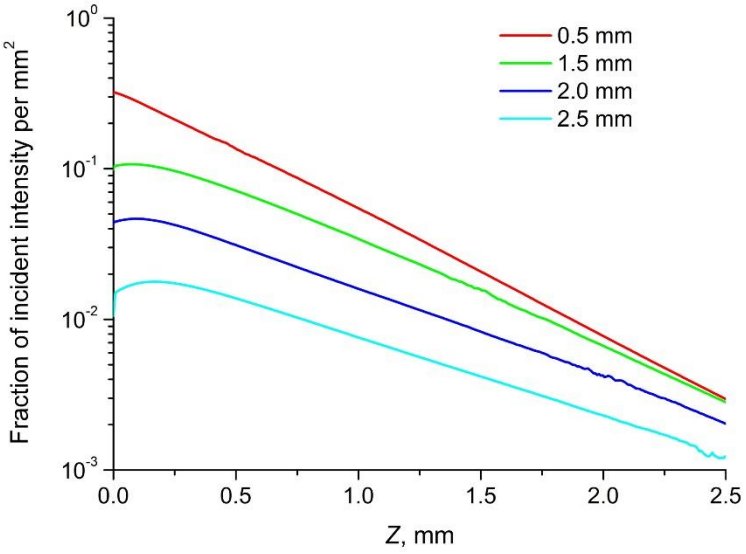

Figure 5: Axial RSOM fluence distribution (conf. *i*) for different FPs.

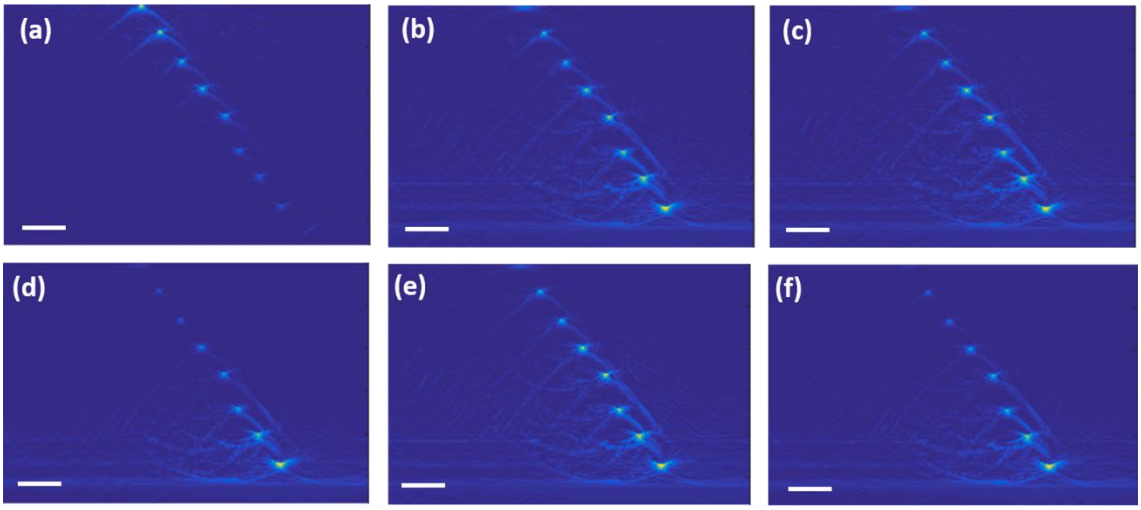

Figure 6: B-scans of the phantom obtained by RSOM system with focus positions at the depth of 2.21 mm under the surface: uncompensated image (a) and images compensated for Monte Carlo simulated RSOM fluence distribution for different optical parameters (b-f) correspond to Table 2. All bars are 1 mm.

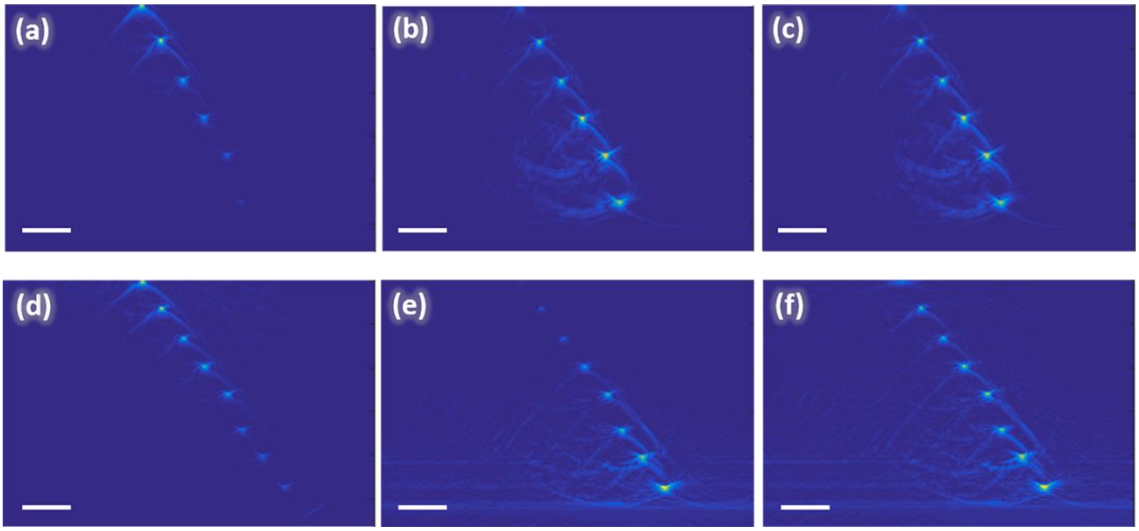

Figure 7: B-scans of the phantom obtained by RSOM system with focus positions at the depth of 1.1 mm (a, b, c) and at the depth of 2.205 mm (d, e, f) under the surface: uncompensated (left column), compensated for exponential fluence distribution (central column), and compensated for Monte Carlo simulated RSOM fluence distribution (right column). All bars are 1 mm.

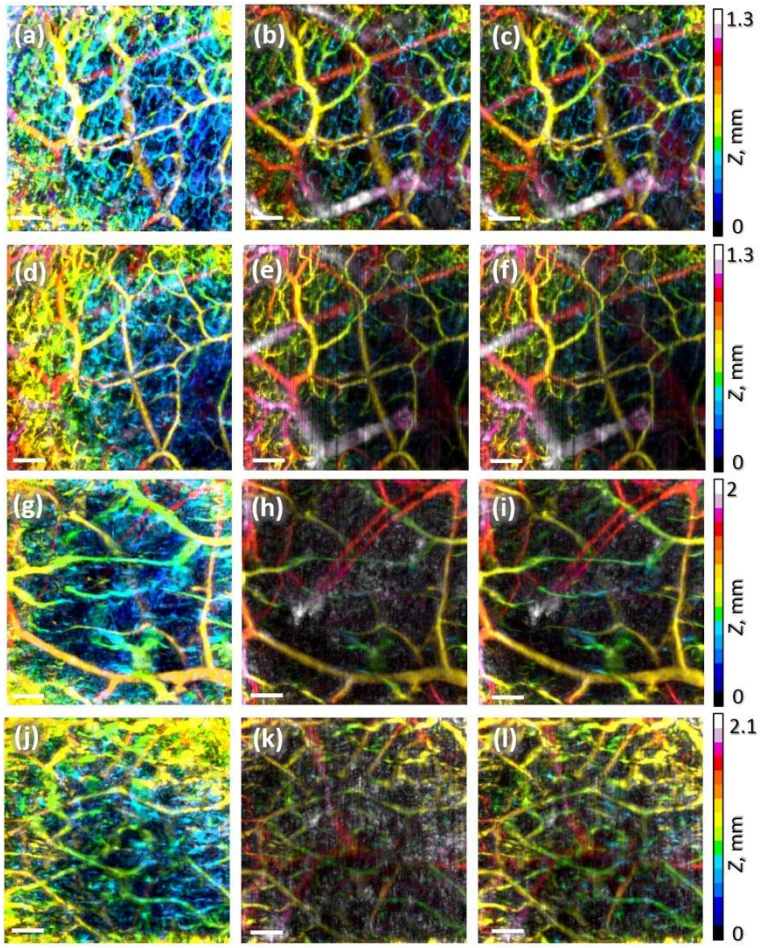

Figure 8: Depth-color-encoded RSOM images of human palm vasculature with focus position on the tissue surface (a, b, c), at the depth of 0.5 mm (d, e, f) and at the depth of 1.5 mm (g, h, i, j, k, l): uncompensated (left column), compensated for exponential fluence distribution (central column), and compensated for Monte Carlo simulated RSOM fluence distribution (right column). All bars are 1 mm.

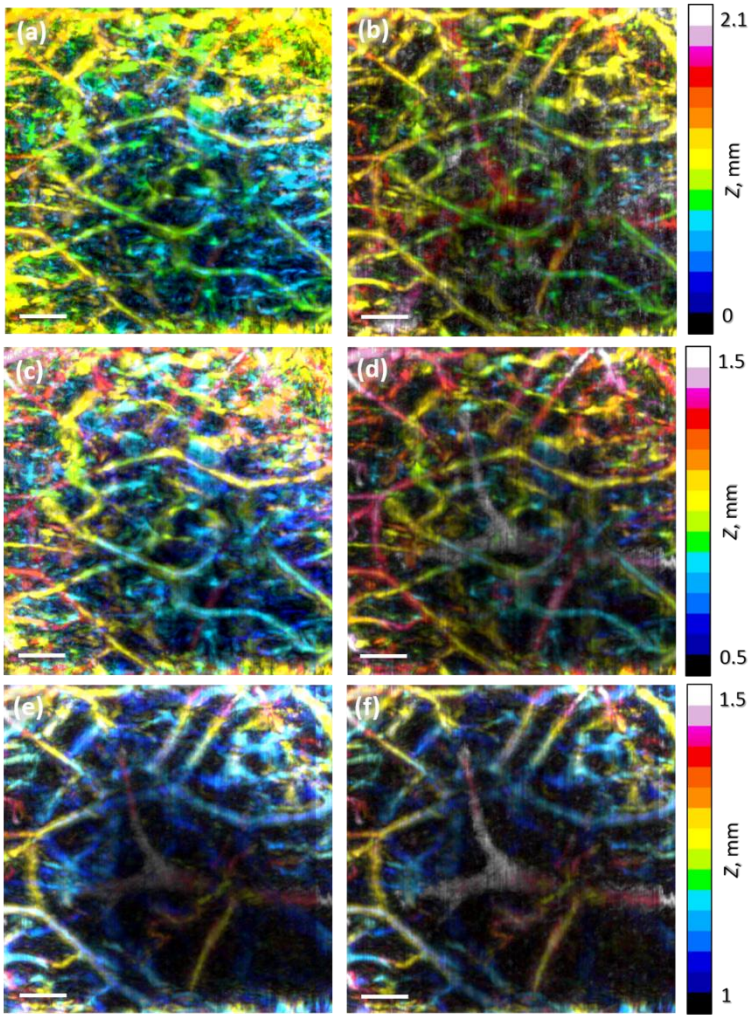

Figure 9: Depth-color-encoded RSOM images of human palm vasculature with focus position at the depth of 1.5 mm at depths from 0 to 2.1 mm (a, b), at depths from 0.5 to 1.5 mm (c, d) and at depths from 1 to 1.5 mm (e, f): uncompensated (left column), compensated for Monte Carlo simulated RSOM fluence distribution (right column). All bars are 1 mm.

Table 1: Optical properties of human skin in the spectral range of 500-600 nm taken from [27, 28].

Tissue type	λ, nm	μ_a, cm^{-1}	μ_s, cm^{-1}	μ_s', cm^{-1}	g
Dermis	500	0.837	9.224	-	0.715
	550	0.786	7.722	-	0.715
	600	0.694	6.309	-	0.715
Dermis	500	0.336 (0.43)	-	4.62 (4.6)	-
	514	0.31 (0.4)	-	4.32 (4.1)	-
	520	0.30 (0.4)	-	4.20 (3.9)	-
	570	0.22 (0.3)	-	3.50 (3.1)	-
	600	0.172 (0.24)	-	3.22 (2.9)	-
Caucasian bloodless dermis	500	0.345	11.99	-	0.120
	550	0.228	10.81	-	0.288
	600	0.181	9.738	-	0.410
Dermis	514	0.3	25	58	0.77
	585	0.3	19.6	41	0.79
Dermis	517	0.22	21	-	0.787
	585	0.22	20.5	-	0.790
	590	0.22	20	-	0.800
	595	0.22	20	-	0.800
	600	0.22	20	-	0.800

Table 2: Optical properties used for Monte Carlo modeling for RSOM phantom measurements.

	Fig. 6 b	Fig. 6 c	Fig. 6 d	Fig. 6 e	Fig. 6 f
μ_a, mm^{-1}	**0.057**	0.0285	0.114	0.057	0.057
μ_s, mm^{-1}	**5.37**	5.37	5.37	2.685	10.74
g	**0.631**	0.631	0.631	0.631	0.631